Article

Oxygen Vacancy-Rich Ultrathin Co$_3$O$_4$ Nanosheets as Nanofillers in Solid-Polymer Electrolyte for High-Performance Lithium Metal Batteries

Qihan Ding [1], Yuhai Dou [2,*], Yunlong Liao [1], Shuhan Huang [1], Rui Wang [1], Wenlu Min [1], Xianghong Chen [1], Chao Wu [2], Ding Yuan [2], Hua Kun Liu [2], Shi Xue Dou [2] and Jiantie Xu [1,3,*]

[1] Guangdong Provincial Key Laboratory of Atmospheric Environment and Pollution Control, National Engineering Laboratory for VOCs Pollution Control Technology and Equipment, School of Environment and Energy, South China University of Technology, Guangzhou 510640, China

[2] Institute of Energy Materials Science, University of Shanghai for Science and Technology, Shanghai 200093, China

[3] School of Physics and Optoelectronics, South China University of Technology, Guangzhou 510640, China

* Correspondence: y.dou@usst.edu.cn (Y.D.); jiantiexu@scut.edu.cn (J.X.)

Abstract: The development of high-performance solid-polymer electrolytes (SPEs) is a key to the practical application of lithium metal batteries (LMBs). The use of two-dimensional (2D) inorganic nanofiller is an efficient way to build poly(ethylene oxide) (PEO)-based SPEs with high ionic conductivity and stability. Herein, a series of 2D oxygen vacancy-rich Co$_3$O$_{4-y}$−x (x = 1, 2 and 3) with well-defined 2D nanostructures, a high surface area and controllable oxygen vacancy contents (Co$_3$O$_{4-y}$) was synthesized via a facile self-assembly method and NaBH$_4$ reduction. When the 2D Co$_3$O$_{4-y}$−x (x = 1, 2 and 3) nanosheets are introduced as nanofillers in PEO-based SPEs, they can interact with the PEO to form a three-dimensional (3D) PEO/Co$_3$O$_{4-y}$ film with uniform Li$^+$ distribution and vertical diffusion channels, as well as strong adsorption of NO$_3^-$ from LiNO$_3$ electrolyte salt at the defective sites. As a result, the PEO/Co$_3$O$_{4-y}$−2 film reached a high ionic conductivity of 4.9 × 10^{-5} S cm^{-1}, high Li$^+$ a transference number of 0.51 and a wide electrochemical window over 4.6 V at 80 °C. The PEO/Co$_3$O$_{4-y}$−2 film enables the Li||PEO/Co$_3$O$_{4-y}$−2||LiFePO$_4$ cell to deliver a high reversible capacity of 117.7 mAh g^{-1} at 2 C and to maintain 126.7 mAh g^{-1} at 1 C after 250 cycles with an initial capacity retention of 87.9%.

Keywords: solid-polymer electrolyte; 2D nanosheets; lithium metal batteries; defect regulation

1. Introduction

Owing to the use of metallic lithium metal as an anode with the ultrahigh theoretical specific capacity of 3860 mAh g^{-1} and low redox potential of −3.04 V vs. Li$^+$/Li, lithium metal batteries (LMBs) have been widely regarded as one of the most promising advanced energy storage systems [1]. The easy formation of lithium dendrites on the metallic lithium metal during cycling and their high sensitivity to traditional organic liquid electrolytes containing flammable and volatile organic solvents, however, can cause an explosion, thermodynamic instability and a shortened cycling life [2]. As expected, the development of alternative electrolytes to traditional liquid electrolytes is a key to the practical application of LMBs. The use of solid-state electrolytes (SSEs) for LMBs has been considered an effective way. This is because the SSEs with a wide electrochemical window and strong mechanical properties not only guarantee the delivery of high-energy density and excellent cycling stability, but also provide a strong physical block to suppress the growth of lithium dendrites [3].

Since the alkali metal salts were dissolved in polyethylene oxide (PEO) by Fenton in 1973 to form conductive complexes [4], using PEO as a polymer matrix to fabricate solid

polymer electrolytes (SPEs) has been intensively investigated. This is mainly due to the PEO-based SPEs with good viscoelasticity, flexible geometry and high ion dissociation ability [5,6]. Despite these, the ionic conductivity of the PEO-based SPEs at room temperature is only 10^{-8}–10^{-7} S cm^{-1}, which makes their practical applications difficult [3]. As a result, many strategies have been developed to improve the ionic conductivity of SPEs, as well as other properties of SPEs. For example, the use of inorganic nanofillers (e.g., Al_2O_3 [7,8], TiO_2 [9], CeO_2 [10], ZrO_2 [11]) into the SPEs can result in the reduced crystallinity of PEO, the decreased interfacial resistance between SPEs and electrodes and the improved ionic conductivity of SPEs. Moreover, the introduction of Lewis acid sites on the surface of nanofillers can adsorb and interact with the anions of the lithium salt, thus leading to an increased number of free Li$^+$ for diffusion and an improved ionic conductivity [12,13]. Apart from the introduction of nanofiller or its surface modification, the morphology control of nanofillers with zero-dimensional (0D, e.g., Al_2O_3 [7,8] and ZnO [14]), one-dimensional (1D, e.g., CeO_2 nanotubes [10], carbon nanotubes [15] and $Li_{0.33}La_{0.557}TiO_3$ (LLTO) nanowires [16]), two-dimensional materials (2D, e.g., graphene oxide [17], g-C_3N_4 [18] and BN flakes [19,20]) or three dimensional (3D, e.g., LLTO frameworks and 3D interconnecting palygorskite network) patterns have also been considered as an efficient way to further enhance the electrochemical and physical properties of SPEs [21]. Among these, 2D nanofillers in SPEs with a large surface area and rich active sites easily interact with PEO so that it can enhance the amorphous phase of SPEs with high-ion mobility [22]. Further, the addition of 2D nanofiller leads to the formation of cross-linked PEO chains in the perpendicular direction, which could facilitate the fast transference of Li$^+$ in the vertical direction [23]. Therefore, it is highly desirable to develop 2D nanofiller in SPEs with rich active sites for high-performance LMBs.

Owing to its exceptionally excellent redox properties and low cost, Co_3O_4 has been intensively investigated and regarded as one of the most important and popular transition metal oxides (TMOs) in various fields such as energy storage/conversion systems and ORR/OER/HER [24,25]. In addition, its intrinsic semiconductor nature further makes it an attractive inorganic nanofiller for SPEs. The defect engineering of Co_3O_4 can significantly optimize the electrocatalytic activities, such as OER [26,27] and CO_2 photoreduction [28]. However, studies on the role of oxygen vacancy in Co_3O_4 to enhance the SPEs properties remain rare and its mechanism also remains unclear [10,13]. Herein, we synthesized a series of Co_3O_4 with well-defined 2D nanostructures, a large surface area and controllable oxygen vacancy contents (Co_3O_{4-y}) via a facile self-assembly synthesis method and $NaBH_4$ reduction, as shown in Figure 1a. The oxygen vacancy contents (y) of $Co_3O_{4-y}-x$ (x = 1, 2 and 3) nanosheets were controlled by controlling $NaBH_4$ with different molar concentrations (x = 1, 2 and 3 standing for 0.05, 0.1 and 0.2 M) in a $Co_3O_4/NaBH_4$ water solution. When the 2D $Co_3O_{4-y}-x$ (x = 1, 2 and 3) nanosheets were used as nanofillers, they could interact with PEO polymer and $LiNO_3$ as an electrolyte additive to form 3D PEO/Co_3O_{4-y} films with uniform distribution of Li$^+$ and their vertical diffusion channels. Moreover, the presence of oxygen vacancy in Co_3O_4 can strongly adsorb NO_3^- at the defective sites in order that it can liberate more free Li$^+$ for diffusion [29]. As a result, the ionic conductivity and Li$^+$ transference number of the PEO/Co_3O_{4-y} film with the optimized oxygen vacancy content (x = 2) could reach 4.9×10^{-5} S cm^{-1} and 0.51 at 80 °C, respectively. When the PEO/$Co_3O_{4-y}-2$ film was applied in the Li||PEO/$Co_3O_{4-y}-2$||Li symmetric cell, the cell exhibited a low polarization voltage of <0.1 V over 800 h at a current density of 0.1 mA cm^{-2} with a limited specific capacity of 0.1 mAh cm^{-2}. In addition, the PEO/$Co_3O_{4-y}-2$ electrolyte enabled the asymmetric cell of the $LiFePO_4$||PEO/$Co_3O_{4-y}-2$||Li to deliver high initial reversible capacities of 162.9 mAh g^{-1} at 0.1 C and 117.7 mAh g^{-1} at 2 C, and to maintain a high reversible capacity of 126.7 mAh g^{-1} at 1 C after 250 cycles with an initial capacity retention of 87.9%.
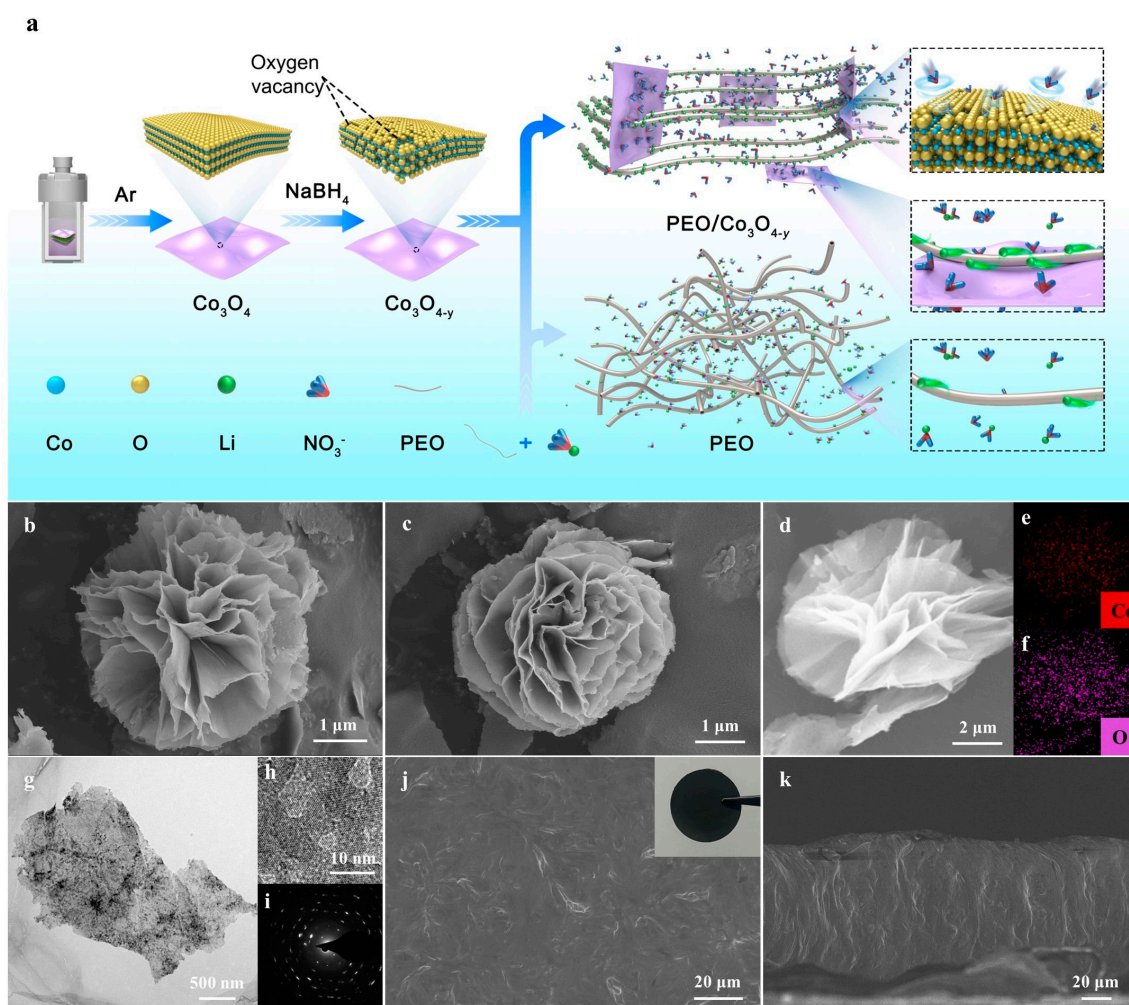
Figure 1. (**a**) Scheme of synthesis route of Co_3O_{4-y} and its interaction with $LiNO_3$ additive and PEO chains. (**b**) Scanning electron microscopy (SEM) image of Co_3O_4. (**c**–**f**) SEM images of $Co_3O_{4-y}-2$ and its corresponding elemental mappings of (**e**) Co and (**f**) O. (**g**,**h**) TEM images and (**i**) SEAD patten of $Co_3O_{4-y}-2$. (**j**) Top-view and (**k**) side-view SEM images of $PEO/Co_3O_{4-y}-2$ electrolyte film.

2. Results and Discussion

The morphology and detailed structures of Co_3O_4 and $Co_3O_{4-y}-x$ ($x = 1, 2$ and 3) nanosheets were characterized by scanning electron microscopy (SEM) and transmission electron microscopy (TEM). As shown in Figure 1b,c, the flower-like Co_3O_4 particle is composed of clear and curved two-dimensional (2D) nanosheets. After defect engineering by $NaBH_4$, the resultant $Co_3O_{4-y}-x$ ($x = 1, 2$ and 3) particles preserve the 2D flower-like and the thin features of Co_3O_4. With the x increase, the $Co_3O_{4-y}-x$ ($x = 3$) becomes agglomerated and even cracked (Figure S1). This is mainly attributed to the etching effect of excessive $NaBH_4$ [30]. Energy dispersive X-ray spectroscopy (EDS) mappings confirm the composition of Co and O as well as their uniform distribution through the nanosheets (Figure 1d–f). The ultrathin feature and crystal structure of $Co_3O_{4-y}-2$ nanosheets were also further confirmed by TEM (Figure 1g) and high-resolution TEM (HRTEM). A HRTEM image of exfoliated $Co_3O_{4-y}-2$ in Figure 1h indicates that the $Co_3O_{4-y}-2$ nanosheet has a high crystallinity with a clear interlayer distance of 0.23 and 0.46 nm between the fringes, which can be attributed to the *d*-space of (222) and (111) crystal plane of spinel Co_3O_4, respectively. Moreover, the ring feature from the corresponding selected area electron diffraction (SAED) pattern in Figure 1i is also well indexed to different crystal planes of spinel Co_3O_4, further confirming the well-defined crystallinity of $Co_3O_{4-y}-2$ (Figure S2). Figures 1j,k and S3 compare the SEM images of PEO and $PEO/Co_3O_{4-y}-2$ electrolyte

films. As can be seen, PEO/Co_3O_{4-y}−2 film has fewer grain boundaries than that of PEO film, indicating its enhanced amorphous feature and the stronger coordination effect between PEO/Co_3O_{4-y}−2 electrolyte film and lithium salts. Furthermore, the side-view SEM images reveal that PEO/Co_3O_{4-y}−2 film presents the well-aligned wrinkled structure perpendicular to its plane compared to the PEO film with a random and dense pattern (Figure 1k and Figure S3). It should be noted that the introduction of PVP to electrolyte film could provide extra porous structures to further enhance the amorphous feature of the electrolyte film, leading to the more flexible SPEs with faster ion transportation [31].

The phases of Co_3O_4 and Co_3O_{4-y}−x (x = 1, 2 and 3) were analyzed by an X-ray diffraction (XRD) technique. As shown in Figure 2a, the diffraction peaks at ~18.9, 31.3, 36.8, 44.8, 59.4 and 65.4° of Co_3O_4 and Co_3O_{4-y}−x (x = 1, 2 and 3) are well indexed into the (111), (220), (311), (400), (511) and (440) planes of cubic Co_3O_4 (JCPDS NO. 42-1467), respectively, indicating the formation of Co_3O_4 with a cubic crystal structure and its chemical stability after the $NaBH_4$ reduction [26]. It should be noted that the larger amorphous regions of Co_3O_{4-y}−x (x = 1, 2 and 3) than Co_3O_4 in the angle range of 11–28° are probably due to the generation of the rich surface edges of the Co_3O_{4-y}−x (x = 1, 2 and 3) during the reduction treatment. Raman spectra in Figure 2b also indicate that four peaks at ~187, 464, 506 and 662 cm^{-1} of Co_3O_4 and Co_3O_{4-y}−x (x = 1, 2 and 3) correspond to the F^1_{2g}, E_{2g}, F^2_{2g} and A_{1g} modes of the Co_3O_4, respectively [32]. As listed in Table S1, the increased full width at half maximum (FWHM) of Co_3O_{4-y}−x (x = 1, 2 and 3) with the x increase is attributed to the increased content of oxygen vacancy induced by $NaBH_4$ etching [33]. To further reveal the oxygen vacancy contents of Co_3O_{4-y}−x (x = 1, 2 and 3), electron paramagnetic resonance (EPR) spectra were carried out. As shown in Figure 2c, the g-value of 2.003 signals caused by the surface oxygen vacancies with an electron trapping of Co_3O_{4-y}−x (x = 1, 2 and 3) increase along with the x increase, indicating the higher x with the richer oxygen vacancies in Co_3O_{4-y}−x (x = 1, 2 and 3) [34]. Furthermore, the N_2 adsorption–desorption isotherm curve and its corresponding specific surface area (Figures 1d and S6) reveal the surface area of Co_3O_4 with 232.6 m^2 g^{-1}, which is higher than that of Co_3O_{4-y}−x (x = 1, 2 and 3) with 167.9, 143.8 and 106.7 m^2 g^{-1}, respectively. As shown in Table S2, the pore volume of Co_3O_{4-y}−x (x = 1, 2 and 3) decreases with the x increase. The lower surface area and pore volume of Co_3O_{4-y}−x (x = 1, 2 and 3) than Co_3O_4 is attributed to the agglomeration of Co_3O_{4-y}−x (x = 1, 2 and 3) nanosheets during the strong $NaBH_4$ reduction.

X-ray photoelectron spectroscopy (XPS) was performed to further evaluate the elemental compositions and their oxidation states of Co_3O_4 and Co_3O_{4-y}−x (x = 1, 2 and 3). As shown in Figures 2e and S5, all materials show the main peaks of Co $2p_{1/2}$ and Co $2p_{3/2}$ located at ~796 and 781 ev, respectively. The Co $2p_{1/2}$ and Co $2p_{3/2}$ peaks of Co_3O_{4-y}−x (x = 1, 2 and 3) have a slightly higher energy shift due to the formation of oxygen vacancies in Co_3O_{4-y} leading to the change in electronic structures of Co_3O_4 [35–37]. The high resolution XPS Co $2p_{1/2}$ and Co $2p_{3/2}$ spectra of all materials can be fitted into the pair peaks Co^{3+}/Co^{2+} at ~780/795 and 781.6/796.8 eV, respectively [28,38]. As listed in Table S1, with the x increase, the intensity ratio of Co^{2+}/(Co^{2+} + Co^{3+}) in the Co_3O_{4-y}−x gradually increases from 58.1% (x = 1) to 68.9% (x = 3), which is much higher than Co_3O_4 of 37.7%, further supporting the formation of oxygen vaccancies in Co_3O_{4-y}−x. Moreover, the O 1s spectra of Co_3O_4 and Co_3O_{4-y}−x (x = 1, 2 and 3) can be deconvoluted into three peaks at ~529.9, 531.3 and 532.6 eV, which are attributed to the lattice oxygen species (O_{Lat}), surface adsorbed oxygen (O_{Ads}) and undesired water molecules (O_{Res}), respectively. As is shown in Table S1, the much higher ratio of O_{Ads}/(O_{Lat} + O_{Ads}) in Co_3O_{4-y}−x (x = 1, 2 and 3) than Co_3O_4, as well as its higher ratio in the Co_3O_{4-y}−x with higher x, once again supports the formation of oxygen vacancies.

Figure 3 shows the structural and morphological analysis of PEO, PEO/Co_3O_4 and PEO/Co_3O_{4-y}−x (x = 1, 2 and 3) electrolyte films. XRD patterns in Figures 3a and S7 show the PEO/Co_3O_4 and PEO/Co_3O_{4-y}−x (x = 1, 2 and 3) films with weaker main characteristic peaks at ~19° and 23° than those of the PEO film, indicating the enhanced amorphous phases of PEO with the addition of Co_3O_4 and Co_3O_{4-y}−x as nanofillers.

Thermogravimetric analysis (TGA) curves of the electrolyte films were measured under air in the temperature range from 100 to 700 °C. As shown in Figure 3b, the initial weight loss of all films below 120 °C is due to the evaporation of water. After 340 °C, the films experience two weight losses in the temperature ranges of 310–360 °C and 360–430 °C, which are assigned to the decomposition of PVP and PEO, respectively [39]. The more relatively smooth PEO/Co_3O_4 and $PEO/Co_3O_{4-y}-x$ (x = 1, 2 and 3) films than the PEO film in these two regions suggest the effective interaction between PEO/PVP and the nanofillers. The difference in the residual mass of the films above 420 °C is mainly attributed to the final products of Co_3O_4 and Li_2CO_3, as evidenced by their XRD patterns (Figure S8). To determine the melting temperatures (T_m) of the electrolyte films, differential scanning calorimetry (DSC) curves were plotted in Figure 3c. Owing to the reduced crystalline and optimized cordinantion of components, the $PEO/Co_3O_{4-y}-2$ film displays the lower T_m of 59.8 °C, followed by PEO/Co_3O_4 (60.8 °C), $PEO/Co_3O_{4-y}-1$ (60.8 °C), $Co_3O_{4-y}-3$ (61.5 °C) and PEO (63.8 °C) films [23].
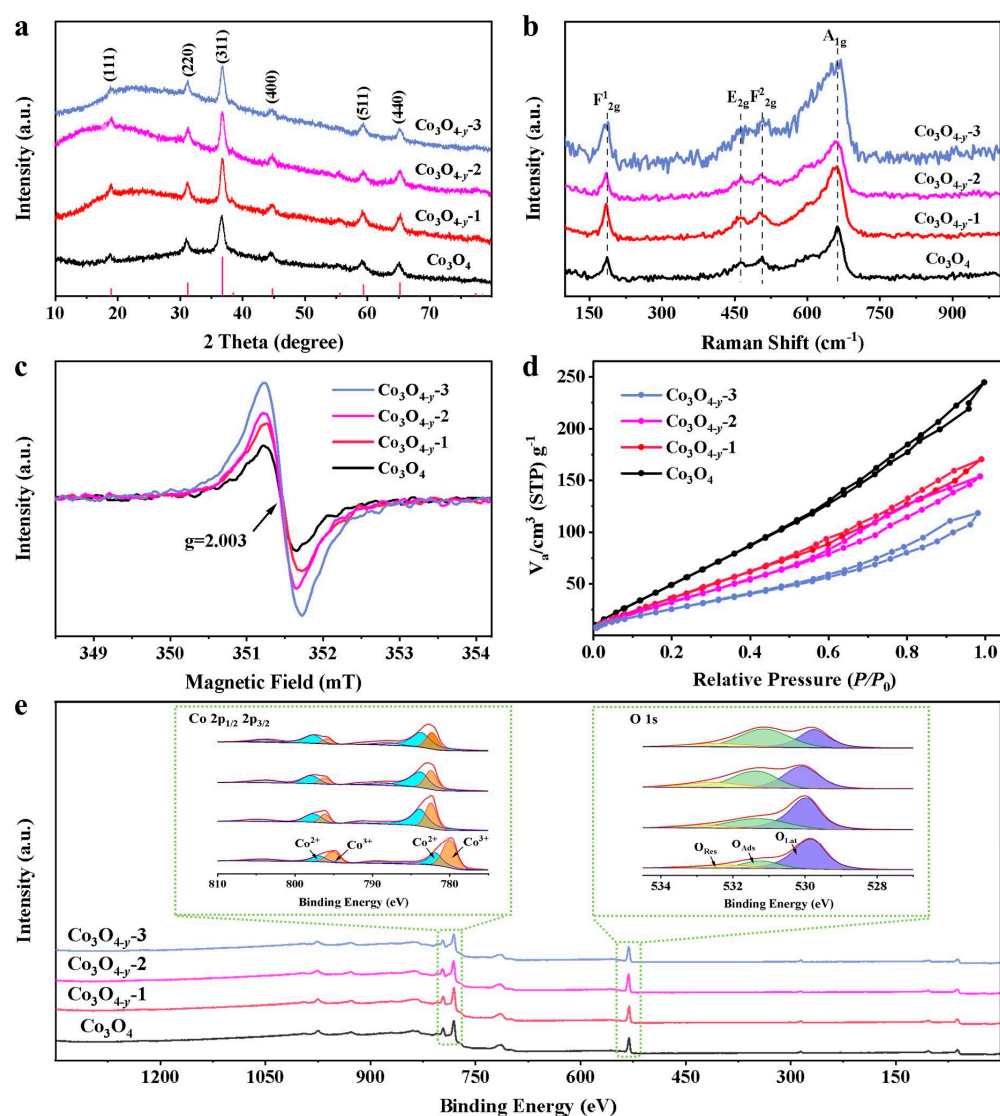
Figure 2. Characterizations of the materials. (**a**) XRD patterns, (**b**) Raman spectra, (**c**) EPR spectra, (**d**) N_2 adsorption–desorption isotherms, and (**e**) XPS spectra of Co_3O_4 and $Co_3O_{4-y}-x$ (x = 1, 2 and 3). Inset of Figure 2e: high resolution XPS Co $2p_{1/2}$ and $2p_{3/2}$, O 1s spectra.
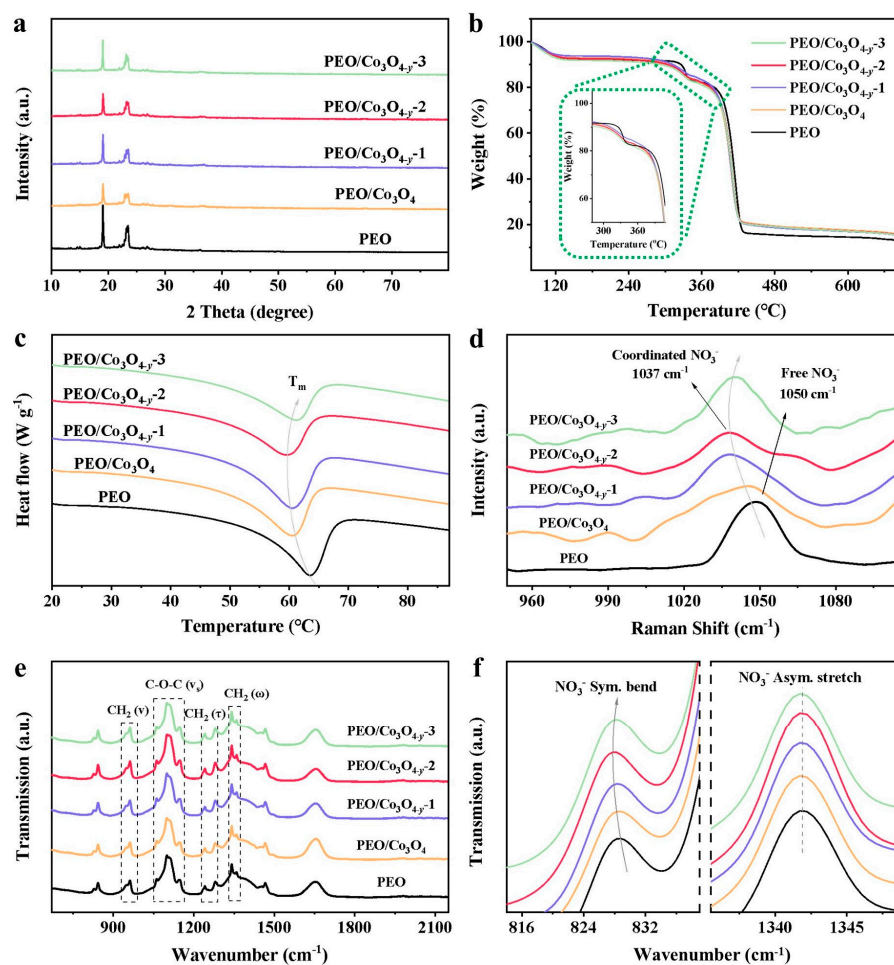
Figure 3. Characterizations of the electrolyte films. (**a**) XRD pattens, (**b**) TGA curves, (**c**) DSC curves, (**d**) Raman spectra, and (**e**,**f**) FTIR spectra of PEO, PEO/Co$_3$O$_4$ and PEO/Co$_3$O$_{4-y}$−x (x = 1, 2 and 3) electrolyte films.

Raman spectra and Fourier transform infrared (FTIR) spectra were further carried out to investigate the interactions between the components of films. Raman spectra in Figure 3d present the increased contents of coordinated NO$_3^-$ at ~1037 cm^{-1} and decreased contents of free NO$_3^-$ at ~1050 cm^{-1} in the PEO/Co$_3$O$_{4-y}$−x (x = 1, 2 and 3) compared to those of PEO/Co$_3$O$_4$ and PEO [40,41]. With the x increase, the increased content of coordinated NO$_3^-$ and decreased content of free NO$_3^-$ were observed. Figure 3e shows the full-survey FTIR spectra of PEO, PEO/Co$_3$O$_4$ and PEO/Co$_3$O$_{4-y}$−x (x = 1, 2 and 3) films with characteristic vibration bands of CH$_2$ (ω) at 1310–1380 cm^{-1}, CH$_2$ (τ) at 1230–1300 cm^{-1}, C-O-C (ν$_s$) at 1000–1150 cm^{-1} and CH$_2$ (ν) at 900–980 cm^{-1} [39]. It should be noted that the FTIR spectra in the range of 1335–1350 and 815–840 cm^{-1} (Figure 3f) are attributed to the signals of asymmetric and symmetric stretching of NO$_3^-$ structures of LiNO$_3$ [42]. The peak position shift of asymmetric and symmetric stretching of NO$_3^-$ indicates the easy dissociation of LiNO$_3$ in the electrolyte films, which is due to the rich oxygen vacancies with abundant Lewis acid sites on Co$_3$O$_4$ surfaces interacting with the free NO$_3^-$ [8,13].

Figure 4 presents the ionic conductivity, Li$^+$ transference number, electrochemical stability and mechanical properties of PEO, PEO/Co$_3$O$_4$ and PEO/Co$_3$O$_{4-y}$−x (x = 1, 2 and 3) films. The ionic conductivities of films were calculated based on the charge transfer resistance in the SS (stainless steel)∣∣SPE∣∣SS cells, which is fitted from the corresponding electrochemical impedance spectra (EIS) together with an equivalent model in Figures 4a and S10. As shown in Figure 4b and listed in Table S3, all films display the improved ionic conductivity with the increasing temperature and the PEO/Co$_3$O$_{4-y}$−2

shows the highest ionic conductivity among the films at each temperature. At 80 and 90 °C, the ionic conductivities of PEO/Co$_3$O$_{4-y}$−2 reach 4.98×10^{-5} and 1.1×10^{-4} S cm^{-1}, respectively. The Li$^+$ transference number (t^+) is also a key indicator of the electrochemical kinetic. The t^+ values were obtained from the chronoamperometry tests of the films in the Li‖SPE‖Li cells at 80 °C with a potential step of 20 mV [43]. Figure 4d shows the highest t^+ value of 0.51 for the PEO/Co$_3$O$_{4-y}$−2 film. It should be noted that the lower t^+ value of PEO/Co$_3$O$_{4-y}$−3 than PEO/Co$_3$O$_{4-y}$−2 is probably due to the overhigh NaBH$_4$ concentration destroying the 2D structure of Co$_3$O$_{4-y}$−3 (Figure S11). The electronic conductivity of PEO, PEO/Co$_3$O$_4$ and PEO/Co$_3$O$_{4-y}$−2 was measured by the DC polarization method at a constant voltage of 0.1 V for 1000 s and calculated by the steady-state current value and the applied external voltage value shown in Figure S12 [44]. As a result, the electronic conductivities of PEO, PEO/Co$_3$O$_4$ and PEO/Co$_3$O$_{4-y}$−2 films are 2.14×10^{-8}, 2.27×10^{-9} and 3.03×10^{-9} S cm^{-1}, respectively, indicating that the introduction of Co$_3$O$_4$ and Co$_3$O$_{4-y}$−2 could reduce the electronic conductivity of the film. This is most likely attributed to the intrinsic semiconductor feature of Co$_3$O$_4$ and Co$_3$O$_{4-y}$−2 even with a low amount of 5 wt.%.
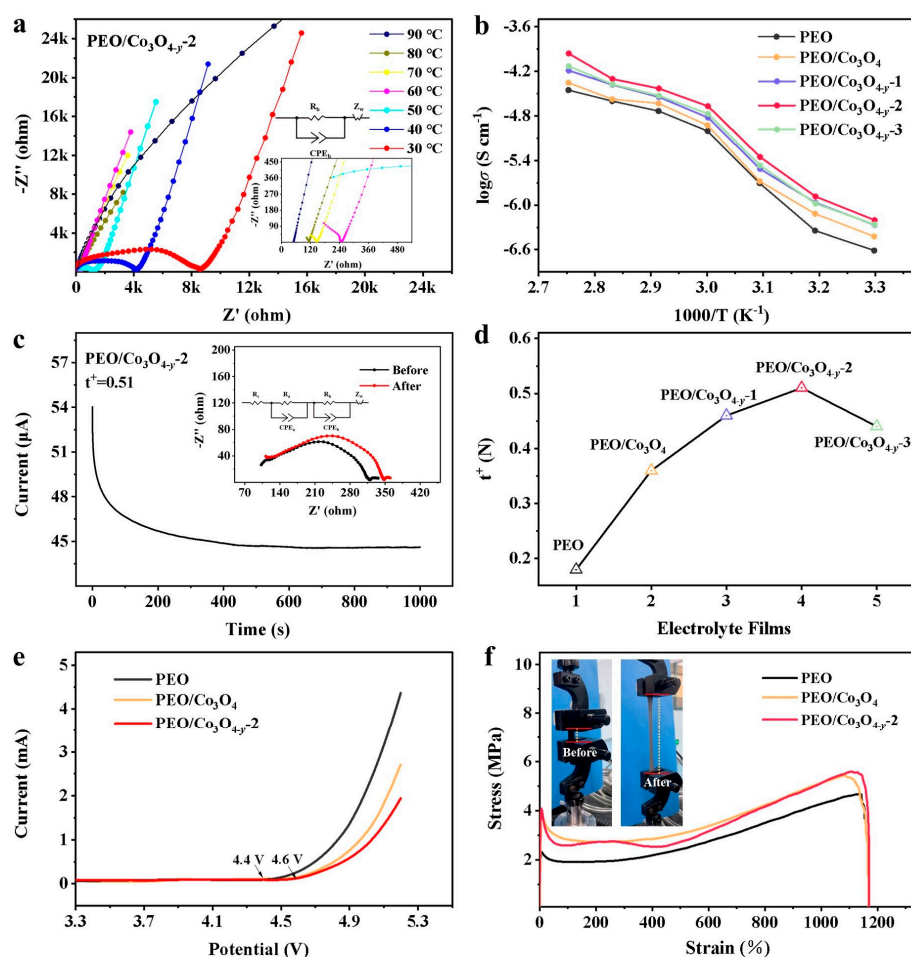
Figure 4. Electrochemical and physical performance of the electrolyte films. (**a**) EIS spectra of symmetric SS‖PEO/Co$_3$O$_{4-y}$−2‖SS cell and (**b**) Arrhenius plots of symmetric SS‖SPEs‖SS cells using PEO, PEO/Co$_3$O$_4$ and PEO/Co$_3$O$_{4-y}$−x (x = 1, 2 and 3) as the electrolyte films, at avarious temperatures from 30 to 90 °C. (**c**) Chronoamperometry curves with a potential step of 20 mV of symmetric Li‖PEO/Co$_3$O$_{4-y}$−2‖Li cell at 80 °C. (**d**) Li$^+$ transference number plot of Li‖SPEs‖Li cells using PEO, PEO/Co$_3$O$_4$ and PEO/Co$_3$O$_{4-y}$−x (x = 1, 2 and 3) as the electrolyte films. (**e**) LSV curves at 0.1 mV s^{-1} of asymmetric SS‖SPEs‖Li cells, and (**f**) stress–strain curves of PEO, PEO/Co$_3$O$_4$ and PEO/Co$_3$O$_{4-y}$−2 films. Inset of Figure 4c: EIS spectra of the cell before and after polarization. Inset of Figure 4f: Digital photos of PEO/Co$_3$O$_{4-y}$−2 at initial and tension states.

To evaluate the electrochemical stability of the electrolyte films, liner sweep voltammetry (LSV) curves of SS||SPEs||Li cells were conducted. As shown in Figures 4e and S1, the cells using PEO/$Co_3O_{4-y}-x$ (x = 1, 2 and 3) and PEO/Co_3O_4 films run stably with a higher oxidative stability >4.6 V than that using PEO film at ~4.4 V. The lower current density of the cells using PEO/$Co_3O_{4-y}-2$ than PEO/Co_3O_4 films at 5.2 V further supports its stronger high-voltage tolerance [45,46]. Figure 4f compares the mechanical properties of the electrolyte films with the stretch rate of 50 mm min^{-1}. As can be seen, all films exhibit the drecreased stress at initial states mainly due to the overcoming of the yield point. Despite the similar fracture limit length of the three electrolyte films, the yielding strength of PEO/$Co_3O_{4-y}-2$ and PEO/Co_3O_4 films can reach ~4.0 MPa, which is much higher than that of the PEO film with ~2.1 MPa. After ~1185% stretching, moreover, the tensile strength of PEO/$Co_3O_{4-y}-2$ and PEO/Co_3O_4 films can reach ~5.1 and 5.2 MPa, respectively, which is also much higher than that of the PEO film with ~4.7 MPa, further indicating its stronger mechanical strength.

To examine the electrochemical stability of the electrolyte films against lithium metal, the Li||SPE||Li symmetric cells using PEO, PEO/Co_3O_4 and PEO/$Co_3O_{4-y}-2$ as electrolyte films were assessed at various current densities from 0.02 to 0.30 mA cm^{-2} at 80 °C. As shown in Figure 5a, the PEO/$Co_3O_{4-y}-2$ displays the lowest polarization at each current density among all the films. At 0.1 mA cm^{-2}, the PEO/$Co_3O_{4-y}-2$ can run more stably in a much lower polarization (<0.1 V) for 800 h without a short circuit (Figure 5b), compared to those of the PEO/Co_3O_4 (<0.16 V) and PEO (<0.2 V) with only 429 and 318 h, respectively. The enhanced cycling stability of the films can also be confirmed by the lithium metal of Li||PEO/$Co_3O_{4-y}-2$||Li cell after cycling for 100 and 318 h with much more smooth surfaces and uniform deposition of lithium dendrites than that of the Li||PEO||Li cell as evidenced by SEM images of the cycled lithium metal surface (Figure 5c–f).

In order to further evaluate the practical feasibility of the electrolyte films, the LiFePO$_4$||SPE||Li asymmetric cells were assembled by using commerical LiFePO$_4$ as the cathode, metallic lithium metal as the anode, and PEO, PEO/Co_3O_4 or PEO/$Co_3O_{4-y}-x$ (x = 1, 2 and 3) as the electrolyte films. Figure 5g,h compares the rate performance of the LiFePO$_4$||SPE||Li cells at various C-rates from 0.1 to 2 C (1 C = 170 mA h g^{-1}) in the voltage range of 2.4–4.0 V. As can be seen, all the cells show the typical charge–discharge behaviours of LiFePO$_4$ with the characteristic flat plateaus at ~3.5 V. The LiFePO$_4$||SPE||Li cell using PEO/$Co_3O_{4-y}-2$ delivers a higher discharge capacity of 165.5 mAh g^{-1} and lower electrode polarization but a lower initial Coulombic efficiency (CE, 78.6%), compared to those using PEO (132 mAh g^{-1} and 92.5%) and PEO/Co_3O_4 (162.7 mAh g^{-1} and 87.6%). The low initial CE is probably due to the formation of the irreversible interface between electrolytes and LiFePO$_4$. In the PEO/$Co_3O_{4-y}-2$ electrolyte film, additional Li$^+$ probably take part in interface formation due to the exsistence of Co_3O_{4-y} nanoparticles [47]. Among the LiFePO$_4$||SPE||Li cells using the PEO/$Co_3O_{4-y}-x$, the PEO/$Co_3O_{4-y}-2$ exhibits the strongest rate capability and delivers the highest average reversible capacities of 169.9, 162.3, 153.8, 147.2 and 116.1 mAhg^{-1} at 0.2, 0.5, 0.8, 1 and 2 C, respectively [48]. The relatively long-term cycling performance of LiFePO$_4$||PEO/$Co_3O_{4-y}-2$||Li cells at 1 C and 2 C in Figure 5j and Figure S14 shows the excellent cycling stability of the cell using PEO/$Co_3O_{4-y}-2$, as well as its superiority to that using PEO/$Co_3O_{4-y}-1$. This is also evidenced by the cell using PEO/$Co_3O_{4-y}-2$ with a high initial discharge capacity of 144.1 mAh g^{-1} at 1 C with an initial capacity retention of 87.9% over 250 cycles, compared to that of PEO/$Co_3O_{4-y}-1$ with 142.8 mAh g^{-1} and 68.8%. The typical and unchanged charge–discharge curves at different cycles in Figure 5k further imply the stability of the PEO/$Co_3O_{4-y}-2$ film during the charge–discharge process. Finally, We compared the electrochemical performance of previously reported literature as listed in Table S4.
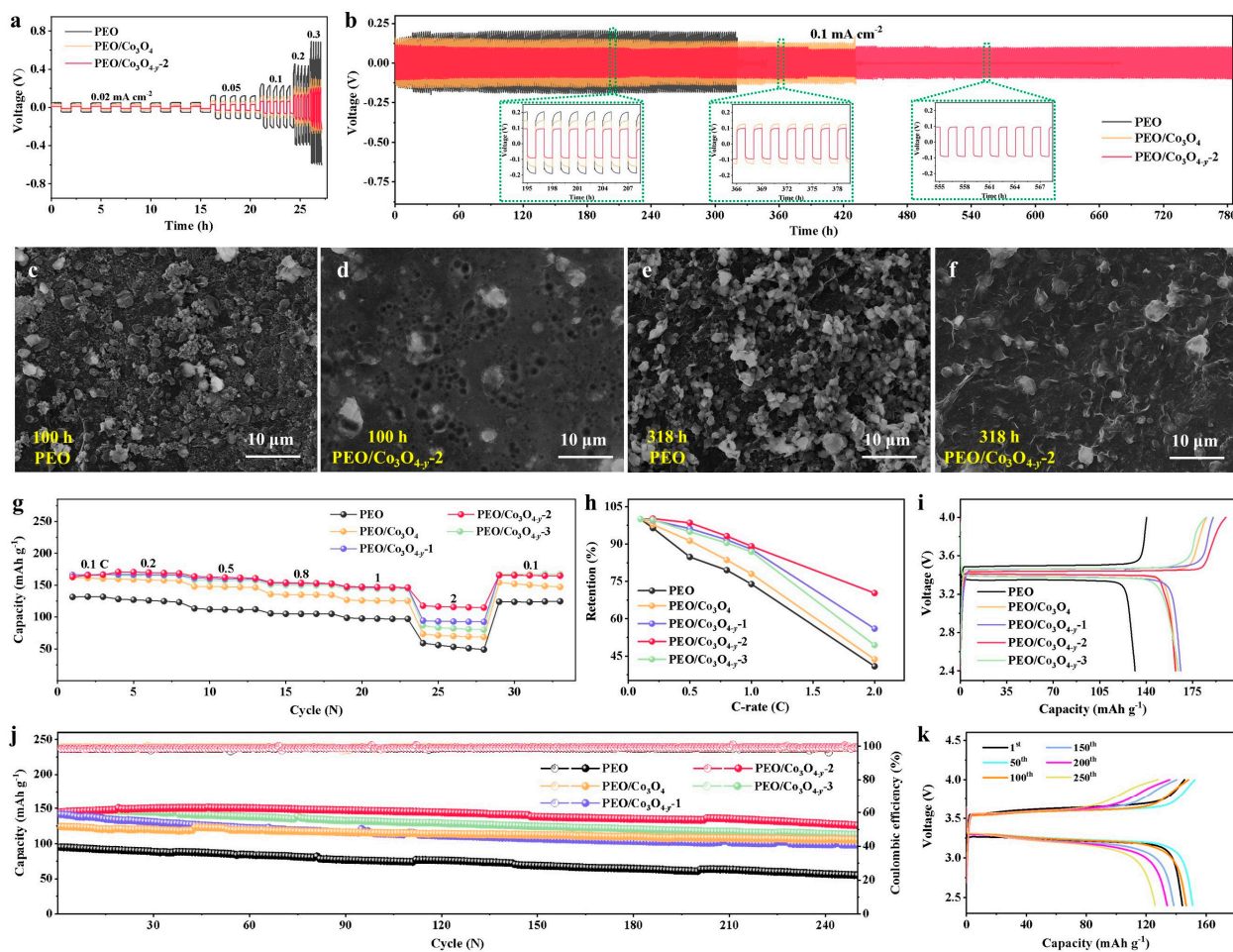
Figure 5. Battery test results of the electrolyte films. (**a**) Rate performance and (**b**) voltage-time profiles of symmetric Li | | SPE | | Li cells using PEO, PEO/Co_3O_4 and PEO/Co_3O_{4-y}−2 electrolyte films. (**c**–**f**) SEM images of Li anode surface with (**c**,**e**) PEO and (**d**,**f**) PEO/Co_3O_{4-y}−2 as the electrolyte films after cycling for 100 and 318 h. (**g**,**h**) Rate performance, (**i**) charge–discharge curves at 0.1 C, and (**j**) cycling performance at 1 C of LiFePO$_4$ | | SPE | | Li cells using PEO, PEO/Co_3O_4 and PEO/Co_3O_{4-y}−x (x = 1, 2 and 3) electrolyte films. (**k**) Charge–discharge curves of the LiFePO$_4$ | | PEO/Co_3O_{4-y}−2 | | Li cell at different cycles.

3. Materials and Methods

3.1. Material Synthesis

Preparation of pristine Co_3O_4 nanosheets: The pristine Co_3O_4 nanosheets were prepared via a self-assembly hydrothermal synthesis method [49]. Typically, 0.4 g Pluronic P123 was dissolved in 6 g ethyl alcohol with a magnetic stirring for 15 min. Then, 16 mL deionized water and 24 mL ethylene glycol (98%, Aldrich) were added to the resultant solution to form an oil–water–surfactant equilibrium system [50]. After stirring for 30 min, 0.26 g Co(CH$_3$COO)$_2$·4H$_2$O and 0.14 g HMTA were added to the equilibrium system. After stirring for 1 h, the pink precursor was obtained and kept without stirring for 24 h, and was then transferred into a hydrothermal reactor and maintained at 160 °C for 15 h. The resultant sample was washed with deionized water five times and dried in a freezer dryer to form the Co_3O_4 nanosheets precursor. Finally, the Co_3O_4 nanosheets precursor was heated at 350 °C for 1 h to obtain the Co_3O_4 nanosheets.

Preparation of oxygen vacancy-rich Co_3O_{4-y} nanosheets: The Co_3O_{4-y}−x (x = 1, 2 and 3) nanosheets with different oxygen vacancy (y) were prepared by using a NaBH$_4$ solution with a different x molar concentration (x = 1, 2 and 3 standing for 0.05, 0.1 and 0.2 M) etching the obtained Co_3O_4 nanosheets. Typically, 0.07 g Co_3O_4 nanosheets were soaked

in 30 mL x NaBH$_4$ solution for 20 min. The black powders (named Co$_3$O$_{4-y}$−x) were then collected by centrifugation, washed in deionized water and freeze-dried.

Preparation of the electrolyte films: The PEO/Co$_3$O$_4$ and PEO/Co$_3$O$_{4-y}$−x (x = 1, 2 and 3) films were fabricated by mixing PEO (M$_w$ = 1 × 10^6, Aldrich), LiNO$_3$ (99%, Aldrich), polyvinyl pyrrolidone (PVP, M$_w$ = 5 × 10^4, Aldrich) and Co$_3$O$_4$ (Co$_3$O$_{4-y}$−x (x = 1, 2 and 3)) in the methanol solvent in a weight ratio of 80:10:14:5 to form a homogeneous solution. The obtained solution was then cast onto a polytetrafluoroethylene (PTEE) plate and dried in a vacuum oven at 60 °C for 24 h. The collected electrolyte films were named as PEO/Co$_3$O$_4$ and PEO/Co$_3$O$_{4-y}$−x (x = 1, 2 and 3). For comparison, the PEO electrolyte was prepared by the same method without using Co$_3$O$_4$ and Co$_3$O$_{4-y}$−x (x = 1, 2 and 3). Before the mechanical and electrochemical test, all the electrolyte films were stored in an argon-filled glove box for seven days to remove the residual methanol.

3.2. Material Characterization

X-ray diffraction (XRD) patterns were measured on a Bruker D8 advance diffractometer with a Cu–Kα radiation (λ = 1.5406 Å). The morphologies and elemental mappings of the materials were characterized by field emission scanning electron microscopy (FE-SEM, Merlin, Zeiss) and transmission electron microscopy (TEM, FEI Talos-F200S). Raman spectra were recorded on a Raman spectrometer (Thermo Fischer DXR). Fourier transform infrared (FTIR) spectroscopy was recorded on a Thermo iS50 in the range of 2200–600 cm^{-1}. Nitrogen adsorption–desorption isotherms were obtained from BELSORP-max (Micro for Tristar II Plus 2.02) and analyzed by using the Barrett–Joyner–Halenda (BJH) method. X-ray photoelectron spectra (XPS) measurements were performed on an Escalab 250Xi X-ray photoelectron spectrometer using C 1s (B.E. = 284.8 eV) as a reference. Electron paramagnetic resonance (EPR) spectra were obtained using a JEOL (FA200) EPR spectrometer at 123.15 K. TGA was carried out on a STA 449 F5 TG analyzer at N$_2$ atmosphere in the temperature range of 100–700 °C with a heating rate of 5 °C min^{-1}. The melting temperature of the electrolyte films was determined by differential scanning calorimetry (DSC, DSC 214 Polyma, Bavaria, Germany).

3.3. Electrochemical Measurements

The electrochemical measurements of the symmetric (e.g., Li(electrode)||SPE (electrolyte)||Li(electrode) and stainless steel (SS)||SPE||SS) and asymmetric cells (e.g., LiFePO$_4$||SPE||Li and SS||SPE||Li) were fabricated in 2032-type coin cells. The LiFePO$_4$ cathode was prepared by mixing 80 wt.% LiFePO$_4$, 10 wt.% super P and 10 wt.% PEO binder in the methanol solution. The resultant slurry, after being stirred for 24 h, was coated in an aluminum foil. The foil was then dried in a vacuum oven at 70 °C for 12 h. Finally, it was punched to a diameter of 11 mm and then transferred into an Ar-filled glove box. The mass of the punched LiFePO$_4$ electrode was controlled with 1.2 mg cm^{-2}. The symmetric and asymmetric cells were assembled in an Ar-filled glove box.

The lithium transference number (t^+) of the electrolyte films was measured in Li||SPEs||Li cells by combining AC impedance and chronoamperometry with 20 mV as the applied potential. Electrochemical impedance spectroscopy (EIS) spectra of the cells were measured from 0.1 to 10^6 Hz before and after polarization. The t^+ values of the electrolyte films were calculated according to the equation [51]:

$$t^+ = \frac{I_{SS}(\Delta V - I_0 R_0)}{I_0(\Delta V - I_{SS} R_{SS})} \tag{1}$$

where I_0 and I_{SS} are the initial and steady-state current, and R_0 and R_{SS} represent the resistance before and after polarization (ΔV = 20 mV), respectively. The ionic/electronic conductivities of the electrolyte films were evaluated by EIS measurements with the frequency range of 0.1–10^6 Hz in the temperature range of 30–90 °C. The electrolyte films

were sandwiched between two stainless steel (SS) disks and the equation for calculating the ionic/electronic conductivity is described as follows:

$$\delta = \frac{l}{R_b S} \tag{2}$$

where l represents the thickness of the SPEs, R_b and S are the bulk resistance of the electrolyte films and the surface area of the electrodes, respectively. The electrochemical tests (EIS and chronoamperometry) of symmetric and asymmetric cells were carried out using a CHI 760C (CH Instruments, Shanghai, China). The coin cells were charged–discharged by using an automatic battery tester system (Land®, Wuhan, China).

4. Conclusions

In summary, a series of two-dimensional (2D) $Co_3O_{4-y}-x$ (x = 1, 2 and 3) with controllable oxygen vacancy contents were fabricated via a facile self-assembly synthetic method and $NaBH_4$ reduction. The 2D $Co_3O_{4-y}-x$ (x = 1, 2 and 3) endow the PEO/$Co_3O_{4-y}-x$ electrolyte films, the uniform distribution of Li^+, its vertical diffusion channels to shorten the diffusion length, and the oxygen vacancy on Co_3O_4 surfaces to strongly adsorb NO_3^- at the defective sites in order that it can liberate more free Li^+ for diffusion. As a result, the PEO/$Co_3O_{4-y}-2$ film reaches the high ionic conductivity of 4.9×10^{-5} S cm^{-1}, a high Li^+ transference number of 0.51 and a wide electrochemical window over 4.6 V at 80 °C. The LiFePO$_4$||PEO/$Co_3O_{4-y}-2$||Li cell displays excellent lithium storage properties with a high initial discharge capacity of 143.9 mAh g^{-1} at 1 C and an initial capacity retention of 87.9% after 250 cycles. This work develops the use of Co_3O_{4-y} nanosheets with oxygen vacancies as nanofillers to build strong mechanical and more flexible SPEs for high-performance lithium metal batteries.

Supplementary Materials: The following supporting information can be downloaded at: https://www.mdpi.com/article/10.3390/catal13040711/s1, Figure S1: SEM images of (a,b) $Co_3O_{4-y}-1$ and (c,d) $Co_3O_{4-y}-3$; Figure S2: (a,b) TEM images and (c) SEAD pattern of Co_3O_4; Figure S3: (a) Top-view and (b) side-view SEM images of PEO electrolyte film; Figure S4: (a) SEM image of PEO/$Co_3O_{4-y}-2$, (b) enlarged SEM image of rectangular frame; Figure S5: XPS survey spectra of Co_3O_4 and $Co_3O_{4-y}-x$ (x = 1, 2 and 3); Figure S6: (a) BET specific surface area and (b) pore size distribution of Co_3O_4 and $Co_3O_{4-y}-x$ (x = 1, 2 and 3); Figure S7: XRD patterns of LiNO$_3$, PVP, PEO and PEO film; Figure S8: XRD pattern of the final residual of PEO/$Co_3O_{4-y}-2$ after TGA. Figure S9: Digital photos of PEO, PEO/Co_3O_4, PEO/$Co_3O_{4-y}-1$, PEO/$Co_3O_{4-y}-2$ and PEO/$Co_3O_{4-y}-3$ films at (a) 25 °C and (b) 80 °C; Figure S10: EIS spectra of symmetric SS||SPEs||SS cells using (a,b) PEO, (c,d) PEO/Co_3O_4, (e,f) PEO/$Co_3O_{4-y}-1$, (g,h) PEO/$Co_3O_{4-y}-2$ and (i,j) PEO/$Co_3O_{4-y}-3$ as electrolyte films at 30–90 °C; Figure S11: Chronoamperometry curves with a potential step of 20 mV of symmetric Li||SPEs||Li cells using (a) PEO, (b) PEO/Co_3O_4, (c) PEO/$Co_3O_{4-y}-1$ and (d) PEO/$Co_3O_{4-y}-3$ as electrolyte films. Inset: EIS spectra of the cell before and after polarization; Figure S12: Polarization current–time curve of PEO, PEO/Co_3O_4 and PEO/$Co_3O_{4-y}-2$ film with an applied external voltage of 0.1 V; Figure S13: LSV curves at 0.1 mV s^{-1} of asymmetric SS||SPEs||Li cells using (a) PEO/$Co_3O_{4-y}-1$, (b) PEO/$Co_3O_{4-y}-3$ as electrolyte films; Figure S14: Cycling performance of Li||PEO/$Co_3O_{4-y}-2$||LiFePO$_4$ cell at 2 C; Table S1. Detailed XPS and Raman analysis results of Co_3O_4 and $Co_3O_{4-y}-x$ (x = 1, 2 and 3); Table S2: Pore volume and average pore size of Co_3O_4 and $Co_3O_{4-y}-x$ (x = 1, 2 and 3); Table S3: Rct data of symmetric SS||SPEs||SS cells using PEO, PEO/Co_3O_4, PEO/$Co_3O_{4-y}-x$ (x = 1, 2 and 3) as the electrolyte films at 30–90 °C; Table S4: Comparisons of the electrochemical performance between Co_3O_{4-y} and previous reported nanofiller-enhanced SPEs. References [10,13,17,48,52–58] are cited in the supplementary materials.

Author Contributions: Conceptualization, Q.D., Y.D. and J.X.; methodology, Q.D. and Y.L.; software, Q.D. and W.M.; validation, formal analysis, investigation, resources, data curation and writing—original draft preparation, Q.D., Y.L., S.H., W.M., R.W. and X.C.; writing—review and editing, and visualization, Q.D., Y.D., J.X., C.W. and D.Y.; supervision, project administration, funding acquisition, Y.D., H.K.L., S.X.D. and J.X. All authors have read and agreed to the published version of the manuscript.

Data Availability Statement: Data Availability Statements are available in the section "MDPI Research Data Policies" at https://www.mdpi.com/ethics.

Conflicts of Interest: The authors declare no conflict of interest.

References

1. Fan, L.-Z.; He, H.; Nan, C.-W. Tailoring inorganic–polymer composites for the mass production of solid-state batteries. *Nat. Rev. Mater.* **2021**, *6*, 1003–1019. [CrossRef]
2. Liu, B.; Zhang, J.-G.; Xu, W. Advancing Lithium Metal Batteries. *Joule* **2018**, *2*, 833–845. [CrossRef]
3. Zhou, D.; Shanmukaraj, D.; Tkacheva, A.; Armand, M.; Wang, G. Polymer Electrolytes for Lithium-Based Batteries: Advances and Prospects. *Chem* **2019**, *5*, 2326–2352. [CrossRef]
4. Fenton, D.E.; Parker, J.M.; Wright, P.V. Complexes of alkali metal ions with poly(ethylene oxide). *Polymer* **1973**, *14*, 589. [CrossRef]
5. Wang, Z.; Shen, L.; Deng, S.; Cui, P.; Yao, X. 10 μm-Thick High-Strength Solid Polymer Electrolytes with Excellent Interface Compatibility for Flexible All-Solid-State Lithium-Metal Batteries. *Adv. Mater.* **2021**, *33*, 2100353. [CrossRef]
6. Quartarone, E.; Mustarelli, P. Electrolytes for solid-state lithium rechargeable batteries: Recent advances and perspectives. *Chem. Soc. Rev.* **2011**, *40*, 2525–2540. [CrossRef] [PubMed]
7. Kaskhedikar, N.; Paulsdorf, J.; Burjanadze, M.; Karatas, Y.; Roling, B.; Wiemhöfer, H.D. Polyphosphazene based composite polymer electrolytes. *Solid State Ion.* **2006**, *177*, 2699–2704. [CrossRef]
8. Croce, F.; Appetecchi, G.B.; Persi, L.; Scrosati, B. Nanocomposite polymer electrolytes for lithium batteries. *Nature* **1998**, *394*, 456–458. [CrossRef]
9. Croce, F.; Persi, L.; Ronci, F.; Scrosati, B. Nanocomposite polymer electrolytes and their impact on the lithium battery technology. *Solid State Ion.* **2000**, *135*, 47–52. [CrossRef]
10. Chen, H.; Adekoya, D.; Hencz, L.; Ma, J.; Chen, S.; Yan, C.; Zhao, H.; Cui, G.; Zhang, S. Stable Seamless Interfaces and Rapid Ionic Conductivity of Ca–CeO2/LiTFSI/PEO Composite Electrolyte for High-Rate and High-Voltage All-Solid-State Battery. *Adv. Energy Mater.* **2020**, *10*, 2000049. [CrossRef]
11. Croce, F.; Settimi, L.; Scrosati, B. Superacid ZrO_2-added, composite polymer electrolytes with improved transport properties. *Electrochem. Commun.* **2006**, *8*, 364–368. [CrossRef]
12. Wu, N.; Chien, P.-H.; Qian, Y.; Li, Y.; Xu, H.; Grundish, N.S.; Xu, B.; Jin, H.; Hu, Y.-Y.; Yu, G.; et al. Enhanced Surface Interactions Enable Fast Li^+ Conduction in Oxide/Polymer Composite Electrolyte. *Angew. Chem. Int. Ed.* **2020**, *59*, 4131–4137. [CrossRef] [PubMed]
13. Liu, W.; Lin, D.; Sun, J.; Zhou, G.; Cui, Y. Improved Lithium Ionic Conductivity in Composite Polymer Electrolytes with Oxide-Ion Conducting Nanowires. *ACS Nano* **2016**, *10*, 11407–11413. [CrossRef] [PubMed]
14. Xiong, H.-M.; Wang, Z.-D.; Xie, D.-P.; Cheng, L.; Xia, Y.-Y. Stable polymer electrolytes based on polyether-grafted ZnO nanoparticles for all-solid-state lithium batteries. *J. Mater. Chem.* **2006**, *16*, 1345–1349. [CrossRef]
15. Kashiwagi, T.; Du, F.; Douglas, J.F.; Winey, K.I.; Harris, R.H.; Shields, J.R. Nanoparticle networks reduce the flammability of polymer nanocomposites. *Nat. Mater.* **2005**, *4*, 928–933. [CrossRef]
16. Liu, W.; Liu, N.; Sun, J.; Hsu, P.-C.; Li, Y.; Lee, H.-W.; Cui, Y. Ionic Conductivity Enhancement of Polymer Electrolytes with Ceramic Nanowire Fillers. *Nano Lett.* **2015**, *15*, 2740–2745. [CrossRef]
17. Wen, J.; Zhao, Q.; Jiang, X.; Ji, G.; Wang, R.; Lu, G.; Long, J.; Hu, N.; Xu, C. Graphene Oxide Enabled Flexible PEO-Based Solid Polymer Electrolyte for All-Solid-State Lithium Metal Battery. *ACS Appl. Energy Mater.* **2021**, *4*, 3660–3669. [CrossRef]
18. Sun, Z.; Li, Y.; Zhang, S.; Shi, L.; Wu, H.; Bu, H.; Ding, S. g-C_3N_4 nanosheets enhanced solid polymer electrolytes with excellent electrochemical performance, mechanical properties, and thermal stability. *J. Mater. Chem. A* **2019**, *7*, 11069–11076. [CrossRef]
19. Shim, J.; Kim, H.J.; Kim, B.G.; Kim, Y.S.; Kim, D.-G.; Lee, J.-C. 2D boron nitride nanoflakes as a multifunctional additive in gel polymer electrolytes for safe, long cycle life and high rate lithium metal batteries. *Energy Environ. Sci.* **2017**, *10*, 1911–1916. [CrossRef]
20. Yin, X.; Wang, L.; Kim, Y.; Ding, N.; Kong, J.; Safanama, D.; Zheng, Y.; Xu, J.; Repaka, D.V.M.; Hippalgaonkar, K.; et al. Thermal Conductive 2D Boron Nitride for High-Performance All-Solid-State Lithium–Sulfur Batteries. *Adv. Sci.* **2020**, *7*, 2001303. [CrossRef]

21. Zheng, Y.; Yao, Y.; Ou, J.; Li, M.; Luo, D.; Dou, H.; Li, Z.; Amine, K.; Yu, A.; Chen, Z. A review of composite solid-state electrolytes for lithium batteries: Fundamentals, key materials and advanced structures. *Chem. Soc. Rev.* **2020**, *49*, 8790–8839. [CrossRef]

22. Tang, W.; Tang, S.; Zhang, C.; Ma, Q.; Xiang, Q.; Yang, Y.-W.; Luo, J. Simultaneously Enhancing the Thermal Stability, Mechanical Modulus, and Electrochemical Performance of Solid Polymer Electrolytes by Incorporating 2D Sheets. *Adv. Energy Mater.* **2018**, *8*, 1800866. [CrossRef]

23. Xu, J.; Meng, Y.; Ding, Q.; Wang, R.; Gan, T.; Zhang, J.; Lin, Z.; Xu, J. High performance lithium ion electrolyte based on a three-dimensional holey graphene framework cross-linked with a polymer. *J. Mater. Chem. A* **2022**, *10*, 4402–4407. [CrossRef]

24. Li, Y.; Li, F.-M.; Meng, X.-Y.; Li, S.-N.; Zeng, J.-H.; Chen, Y. Ultrathin Co_3O_4 Nanomeshes for the Oxygen Evolution Reaction. *ACS Catal.* **2018**, *8*, 1913–1920. [CrossRef]

25. Li, S.; Liu, Q.; Zhou, J.; Pan, T.; Gao, L.; Zhang, W.; Fan, L.; Lu, Y. Hierarchical Co_3O_4 Nanofiber–Carbon Sheet Skeleton with Superior Na/Li-Philic Property Enabling Highly Stable Alkali Metal Batteries. *Adv. Funct. Mater.* **2019**, *29*, 1808847. [CrossRef]

26. Xiao, Z.; Wang, Y.; Huang, Y.-C.; Wei, Z.; Dong, C.-L.; Ma, J.; Shen, S.; Li, Y.; Wang, S. Filling the oxygen vacancies in Co_3O_4 with phosphorus: An ultra-efficient electrocatalyst for overall water splitting. *Energy Environ. Sci.* **2017**, *10*, 2563–2569. [CrossRef]

27. Xu, L.; Jiang, Q.; Xiao, Z.; Li, X.; Huo, J.; Wang, S.; Dai, L. Plasma-Engraved Co_3O_4 Nanosheets with Oxygen Vacancies and High Surface Area for the Oxygen Evolution Reaction. *Angew. Chem. Int. Ed.* **2016**, *55*, 5277–5281. [CrossRef]

28. Zhang, Q.; Yang, P.; Zhang, H.; Zhao, J.; Shi, H.; Huang, Y.; Yang, H. Oxygen vacancies in Co_3O_4 promote CO_2 photoreduction. *Appl. Catal. B Environ.* **2022**, *300*, 120729. [CrossRef]

29. Zhang, Z.; Wang, J.; Zhang, S.; Ying, H.; Zhuang, Z.; Ma, F.; Huang, P.; Yang, T.; Han, G.; Han, W.-Q. Stable all-solid-state lithium metal batteries with Li3N-LiF-enriched interface induced by lithium nitrate addition. *Energy Storage Mater.* **2021**, *43*, 229–237. [CrossRef]

30. Yan, D.; Wang, W.; Luo, X.; Chen, C.; Zeng, Y.; Zhu, Z. $NiCo_2O_4$ with oxygen vacancies as better performance electrode material for supercapacitor. *Chem. Eng. J.* **2018**, *334*, 864–872. [CrossRef]

31. Zhang, X.; Takegoshi, K.; Hikichi, K. High-resolution solid-state 13C nuclear magnetic resonance study on poly(vinyl alcohol)/poly(vinylpyrrolidone) blends. *Polymer* **1992**, *33*, 712–717. [CrossRef]

32. Zhai, T.; Wan, L.; Sun, S.; Chen, Q.; Sun, J.; Xia, Q.; Xia, H. Phosphate Ion Functionalized Co3O4 Ultrathin Nanosheets with Greatly Improved Surface Reactivity for High Performance Pseudocapacitors. *Adv. Mater.* **2017**, *29*, 1604167. [CrossRef] [PubMed]

33. Wang, Y.; Cai, J.; Wu, M.; Chen, J.; Zhao, W.; Tian, Y.; Ding, T.; Zhang, J.; Jiang, Z.; Li, X. Rational construction of oxygen vacancies onto tungsten trioxide to improve visible light photocatalytic water oxidation reaction. *Appl. Catal. B Environ.* **2018**, *239*, 398–407. [CrossRef]

34. Ji, D.; Fan, L.; Tao, L.; Sun, Y.; Li, M.; Yang, G.; Tran, T.Q.; Ramakrishna, S.; Guo, S. The Kirkendall Effect for Engineering Oxygen Vacancy of Hollow Co_3O_4 Nanoparticles toward High-Performance Portable Zinc–Air Batteries. *Angew. Chem. Int. Ed.* **2019**, *58*, 13840–13844. [CrossRef]

35. Li, R.; Huang, Y.; Zhu, D.; Ho, W.; Cao, J.; Lee, S. Improved Oxygen Activation over a Carbon/Co_3O_4 Nanocomposite for Efficient Catalytic Oxidation of Formaldehyde at Room Temperature. *Environ. Sci. Technol.* **2021**, *55*, 4054–4063. [CrossRef] [PubMed]

36. Dou, Y.; Liao, T.; Ma, Z.; Tian, D.; Liu, Q.; Xiao, F.; Sun, Z.; Ho Kim, J.; Xue Dou, S. Graphene-like holey Co_3O_4 nanosheets as a highly efficient catalyst for oxygen evolution reaction. *Nano Energy* **2016**, *30*, 267–275. [CrossRef]

37. Sun, Y.; Gao, S.; Xie, Y. Atomically-thick two-dimensional crystals: Electronic structure regulation and energy device construction. *Chem. Soc. Rev.* **2014**, *43*, 530–546. [CrossRef] [PubMed]

38. Wang, X.; Li, X.; Mu, J.; Fan, S.; Chen, X.; Wang, L.; Yin, Z.; Tadé, M.; Liu, S. Oxygen Vacancy-rich Porous Co_3O_4 Nanosheets toward Boosted NO Reduction by CO and CO Oxidation: Insights into the Structure–Activity Relationship and Performance Enhancement Mechanism. *ACS Appl. Mater. Interfaces* **2019**, *11*, 41988–41999. [CrossRef]

39. Jinisha, B.; Anilkumar, K.M.; Manoj, M.; Pradeep, V.S.; Jayalekshmi, S.J.E.A. Development of a novel type of solid polymer electrolyte for solid state lithium battery applications based on lithium enriched poly (ethylene oxide) (PEO)/poly (vinyl pyrrolidone) (PVP) blend polymer. *Electrochim. Acta* **2017**, *235*, 210–222. [CrossRef]

40. Romero, M.; Faccio, R.; Mombrú, Á.W. Novel fluorine-free 2,2′-bis(4,5-dimethylimidazole) additive for lithium-ion poly(methyl methacrylate) solid polymer electrolytes. *RSC Adv.* **2016**, *6*, 67150–67156. [CrossRef]

41. Seo, J.; Lee, G.-H.; Hur, J.; Sung, M.-C.; Seo, J.-H.; Kim, D.-W. Mechanically Interlocked Polymer Electrolyte with Built-In Fast Molecular Shuttles for All-Solid-State Lithium Batteries. *Adv. Energy Mater.* **2021**, *11*, 2102583. [CrossRef]

42. Zhao, Q.; Utomo, N.W.; Kocen, A.L.; Jin, S.; Deng, Y.; Zhu, V.X.; Moganty, S.; Coates, G.W.; Archer, L.A. Upgrading Carbonate Electrolytes for Ultra-stable Practical Lithium Metal Batteries. *Angew. Chem. Int. Ed.* **2022**, *61*, e202116214. [CrossRef]

43. Guo, Q.; Xu, F.; Shen, L.; Deng, S.; Wang, Z.; Li, M.; Yao, X. 20 μm-Thick Li6.4La3Zr1.4Ta0.6O12-Based Flexible Solid Electrolytes for All-Solid-State Lithium Batteries. *Energy Mater. Adv.* **2022**, *2022*, 9753506. [CrossRef]

44. Han, F.; Westover, A.S.; Yue, J.; Fan, X.; Wang, F.; Chi, M.; Leonard, D.N.; Dudney, N.J.; Wang, H.; Wang, C. High electronic conductivity as the origin of lithium dendrite formation within solid electrolytes. *Nat. Energy* **2019**, *4*, 187–196. [CrossRef]

45. Siyal, S.H.; Li, M.; Li, H.; Lan, J.-L.; Yu, Y.; Yang, X. Ultraviolet irradiated PEO/LATP composite gel polymer electrolytes for lithium-metallic batteries (LMBs). *Appl. Surf. Sci.* **2019**, *494*, 1119–1126. [CrossRef]

46. Park, C.H.; Kim, D.W.; Prakash, J.; Sun, Y.-K. Electrochemical stability and conductivity enhancement of composite polymer electrolytes. *Solid State Ion.* **2003**, *159*, 111–119. [CrossRef]

47. Li, H.; Du, Y.; Zhang, Q.; Zhao, Y.; Lian, F. A Single-Ion Conducting Network as Rationally Coordinating Polymer Electrolyte for Solid-State Li Metal Batteries. *Adv. Energy Mater.* **2022**, *12*, 2103530. [CrossRef]

48. Wu, X.; Chen, K.; Yao, Z.; Hu, J.; Huang, M.; Meng, J.; Ma, S.; Wu, T.; Cui, Y.; Li, C. Metal organic framework reinforced polymer electrolyte with high cation transference number to enable dendrite-free solid state Li metal conversion batteries. *J. Power Sources* **2021**, *501*, 229946. [CrossRef]

49. Sun, Z.; Liao, T.; Dou, Y.; Hwang, S.M.; Park, M.-S.; Jiang, L.; Kim, J.H.; Dou, S.X. Generalized self-assembly of scalable two-dimensional transition metal oxide nanosheets. *Nat. Commun.* **2014**, *5*, 3813. [CrossRef]

50. Dou, Y.; Zhang, L.; Xu, J.; He, C.-T.; Xu, X.; Sun, Z.; Liao, T.; Nagy, B.; Liu, P.; Dou, S.X. Manipulating the Architecture of Atomically Thin Transition Metal (Hydr)oxides for Enhanced Oxygen Evolution Catalysis. *ACS Nano* **2018**, *12*, 1878–1886. [CrossRef]

51. Evans, J.; Vincent, C.A.; Bruce, P.G. Electrochemical measurement of transference numbers in polymer electrolytes. *Polymer* **1987**, *28*, 2324–2328. [CrossRef]

52. Jung, S.; Kim, D.W.; Lee, S.D.; Cheong, M.; Nguyen, D.Q.; Cho, B.W.; Kim, H.S. Fillers for solid-state polymer electrolytes: Highlight. *Bull. Korean Chem. Soc.* **2009**, *30*, 2355–2361. [CrossRef]

53. Tang, W.; Tang, S.; Guan, X.; Zhang, X.; Xiang, Q.; Luo, J. High-performance solid polymer electrolytes filled with vertically aligned 2D materials. *Adv. Funct. Mater.* **2019**, *29*, 1900648. [CrossRef]

54. Wang, C.; Yang, T.; Zhang, W.; Huang, H.; Gan, Y.; Xia, Y.; He, X.; Zhang, J. Hydrogen bonding enhanced SiO2/PEO composite electrolytes for solid-state lithium batteries. *J. Mater. Chem. A* **2022**, *10*, 3400–3408. [CrossRef]

55. Yang, Z.; Sun, Z.; Liu, C.; Li, Y.; Zhou, G.; Zuo, S.; Wang, J.; Wu, W. Lithiated nanosheets hybridized solid polymer electrolyte to construct Li+ conduction highways for advanced all-solid-state lithium battery. *J. Power Sources* **2021**, *484*, 229287. [CrossRef]

56. Li, C.; Zhou, S.; Dai, L.; Zhou, X.; Zhang, B.; Chen, L.; Zeng, T.; Liu, Y.; Tang, Y.; Jiang, J.; et al. Porous polyamine/PEO composite solid electrolyte for high performance solid-state lithium metal batteries. *J. Mater. Chem. A* **2021**, *9*, 24661–24669. [CrossRef]

57. Nematdoust, S.; Najjar, R.; Bresser, D.; Passerini, S. Understanding the role of nanoparticles in PEO-based hybrid polymer electrolytes for solid-state lithium–polymer batteries. *J. Phys. Chem. C* **2020**, *124*, 27907–27915. [CrossRef]

58. Li, Y.; Sun, Z.; Liu, D.; Gao, Y.; Wang, Y.; Bu, H.; Li, M.; Zhang, Y.; Gao, G.; Ding, S. A composite solid polymer electrolyte incorporating MnO2 nanosheets with reinforced mechanical properties and electrochemical stability for lithium metal batteries. *J. Mater. Chem. A* **2020**, *8*, 2021–2032. [CrossRef]